THE JOURNAL OF BIOLOGICAL CHEMISTRY VOL. 290, NO. 26, pp. 16246–16260, June 26, 2015

Structural Characterization of Phosducin and Its Complex with the 14-3-3 Protein*

Received for publication, January 5, 2015, and in revised form, April 21, 2015 Published, JBC Papers in Press, May 13, 2015, DOI 10.1074/jbc.M115.636563

Miroslava Kacirova[‡§], Dalibor Kosek[‡§], Alan Kadek[¶‖], Petr Man[¶‖], Jaroslav Vecer[**], Petr Herman[**], Veronika Obsilova[§1], and Tomas Obsil[‡§2]

From the Departments of [‡]Physical and Macromolecular Chemistry and [‖]Biochemistry Faculty of Science, Charles University in Prague, 12843 Prague, the Institutes of [§]Physiology and [¶]Microbiology,Czech Academy of Sciences, 14220 Prague, and the [**]Institute of Physics, Faculty of Mathematics and Physics, Charles University in Prague, 12116 Prague, Czech Republic

Background: Phosducin is a conserved regulatory phosphoprotein involved in phototransduction whose function is regulated in a 14-3-3-dependent manner.
Results: The 14-3-3 protein binding affects the structure and the accessibility of several regions within both domains of phosphorylated phosducin.
Conclusion: The 14-3-3 protein sterically occludes the whole $G_t\beta\gamma$ binding interface of phosducin.
Significance: Mechanistic explanation is given for the 14-3-3-dependent inhibition of phosducin function.

Phosducin (Pdc), a highly conserved phosphoprotein involved in the regulation of retinal phototransduction cascade, transcriptional control, and modulation of blood pressure, is controlled in a phosphorylation-dependent manner, including the binding to the 14-3-3 protein. However, the molecular mechanism of this regulation is largely unknown. Here, the solution structure of Pdc and its interaction with the 14-3-3 protein were investigated using small angle x-ray scattering, time-resolved fluorescence spectroscopy, and hydrogen-deuterium exchange coupled to mass spectrometry. The 14-3-3 protein dimer interacts with Pdc using surfaces both inside and outside its central channel. The N-terminal domain of Pdc, where both phosphorylation sites and the 14-3-3-binding motifs are located, is an intrinsically disordered protein that reduces its flexibility in several regions without undergoing dramatic disorder-to-order transition upon binding to 14-3-3. Our data also indicate that the C-terminal domain of Pdc interacts with the outside surface of the 14-3-3 dimer through the region involved in $G_t\beta\gamma$ binding. In conclusion, we show that the 14-3-3 protein interacts with and sterically occludes both the N- and C-terminal $G_t\beta\gamma$ binding interfaces of phosphorylated Pdc, thus providing a mechanistic explanation for the 14-3-3-dependent inhibition of Pdc function.

Phosducin (Pdc)[3] is a highly conserved phosphoprotein involved in the regulation of visual signal transduction, transcriptional control, regulation of transmission at the photoreceptor-to-ON-bipolar cell synapse, and modulation of sympathetic activity and blood pressure (1–5). Other members of the Pdc protein family, Pdc-like proteins, act as co-chaperons and assist in the folding of a variety of proteins (6). The function of Pdc is best understood in the modulation of light-induced processes in rod photoreceptor cells where Pdc assists in the process of shutting down rod responsiveness during prolonged exposure to intense light. Pdc binds to the complex of $\beta\gamma$ subunits of the retinal G protein transducin ($G_t\beta\gamma$), mediates its sequestration to the cytosol, and prevents its re-association with the $G_t\alpha$ subunit of transducin. The binding of Pdc to the $G_t\beta\gamma$ complex is controlled through the phosphorylation of Ser^{54} and Ser^{73} by Ca^{2+}-calmodulin-dependent and cAMP-dependent protein kinases (2, 7–9). However, the phosphorylation of these two sites by itself has only a weak effect on Pdc binding to $G_t\beta\gamma$ in the intact retina, and the efficient inhibition of this interaction requires the presence of the 14-3-3 protein that associates with the phosphorylated Pdc and presumably blocks its interaction with $G_t\beta\gamma$ (9–11). The 14-3-3 proteins are highly conserved dimeric molecules that recognize specific phosphoserine/phosphothreonine-containing motifs. Through these binding interactions, the 14-3-3 proteins regulate functions of other proteins by modulating their structure, masking functional sites on their surfaces, or promoting protein/protein interactions (12). The exact role of the 14-3-3 protein binding in Pdc regulation is, however, still unclear mainly due to the lack of structural data.

The structural analysis of the Pdc·$G_t\beta\gamma$ complex revealed that Pdc consists of two separate domains that are both involved in binding to $G_t\beta\gamma$ (Fig. 1*A*) (13, 14). Whereas the mostly helical N-terminal domain (Pdc-ND) constitutes the main part of Pdc's interaction surface with $G_t\beta\gamma$ (~65% of

* This work was supported by the Czech Science Foundation Project P305/11/0708, Grant Agency of Charles University Project 793913, and Czech Academy of Sciences Research Projects RVO 67985823 of the Institute of Physiology. The authors declare that they have no conflicts of interest with the contents of this article.
[1] To whom correspondence may be addressed. Tel.: 420-241062191; Fax: 420-244472269; E-mail: veronika.obsilova@fgu.cas.cz.
[2] To whom correspondence may be addressed: Tel.: 420-221951303; Fax: 420-224919752; E-mail: obsil@natur.cuni.cz.
[3] The abbreviations used are: Pdc, phosducin; ANS, 8-anilinonaphthalene-1-sulfonic acid; AUC, analytical ultracentrifugation; DLS, dynamic light scattering; HDX-MS, hydrogen-deuterium exchange coupled to mass spectrometry; pPdc, phosphorylated phosducin; Pdc-ND, N-terminal domain of Pdc; pPdc-ND, phosphorylated N-terminal domain of Pdc; Pdc-CD, C-terminal domain of Pdc; SAXS, small angle x-ray scattering; SV, sedimentation velocity; EOM, ensemble optimization method; dansyl, 5-dimethylaminonaphthalene-1-sulfonyl.

the total binding surface) and is responsible for competing with $G_t\alpha$ for $G_t\beta\gamma$, the C-terminal domain (Pdc-CD) possesses the thioredoxin-like fold and seems to be responsible for blocking the interaction of $G_t\beta\gamma$ with the membrane. These structural studies also suggested that Pdc-ND is highly flexible, especially in regions where it does not contact $G_t\beta\gamma$, and in its free state it lacks an explicit native conformation in contrast to the helical conformation observed in the complex with $G_t\beta\gamma$. Phosphorylation sites Ser^{54} and Ser^{73}, which control the binding of Pdc to $G_t\beta\gamma$, are both located within Pdc-ND, and it has been shown that their simultaneous phosphorylation is required for a stable complex formation between phosphorylated Pdc (pPdc) and the 14-3-3ζ protein (15). This suggested that phosphorylation of Ser^{54} and Ser^{73} creates two 14-3-3-binding motifs that are used simultaneously to engage both ligand binding grooves within the 14-3-3ζ protein dimer. The presence of both 14-3-3-binding motifs within Pdc-ND also indicates that this domain constitutes the main part of Pdc's interaction surface with the 14-3-3 protein, which might either sterically block the Pdc's $G_t\beta\gamma$-binding surface and/or change its structure. We have recently shown, using time-resolved dansyl fluorescence spectroscopy, that the 14-3-3ζ protein binding reduces the segmental dynamics within several regions of the dansyl-labeled pPdc molecule, suggesting that pPdc undergoes a conformational change upon binding to 14-3-3ζ (15). These changes involve parts of the $G_t\beta\gamma$ binding surface of Pdc-ND, thus supporting the inhibitory role of the 14-3-3 protein in Pdc binding to $G_t\beta\gamma$. In addition, it has also been speculated that the 14-3-3 protein binding decreases the rate of Pdc dephosphorylation after a light stimulus by virtue of its interaction with phosphorylated Ser^{54} and Ser^{73}, thus lengthening the time that Pdc remains phosphorylated after a light exposure and/or stabilizes the N-terminal domain and protects phosphorylated Pdc from degradation (9). Yet another role for the 14-3-3 protein binding might be in the regulation of Pdc interaction with other proteins, including the SUG1 subunit of the proteasome complex and the transcription factor CRX (3, 16). More detailed structural data on Pdc, of which the unbound (apo) structure is unknown, and its complex with the 14-3-3 protein are clearly needed to better understand the role of 14-3-3 in the regulation of Pdc function.

Here, we use small angle x-ray scattering (SAXS), time-resolved fluorescence spectroscopy, quenching of tryptophan fluorescence, hydrogen-deuterium exchange kinetics coupled with mass spectrometry (HDX-MS), and other biophysical approaches to investigate the solution structure of apo Pdc and its interaction with the 14-3-3ζ protein.

Experimental Procedures

Expression, Purification, and Phosphorylation of Pdc—Rat full-length Pdc (UniProt ID P20942) Q52K mutant doubly phosphorylated at Ser^{54} and Ser^{73} was prepared as described previously (15). Pdc-ND (residues 1–107) was prepared by introducing a stop codon instead of Gly^{108} using the QuikChange kit (Stratagene). The status of Pdc and Pdc-ND phosphorylation was examined by mass spectrometry. Pdc-CD was prepared by ligating the cDNA encoding sequence 110–246 into pET-15b (Novagen) using the NdeI and BamHI sites. The entire coding region was checked by sequencing. Both Pdc-ND and Pdc-CD were expressed as His_6-tagged proteins and purified using the same protocol as full-length Pdc.

Expression and Purification of 14-3-3ζ—The mutant version of the 14-3-3ζ protein (human isoform ζ) containing no tryptophan residues (mutations W59F and W228F, denoted as 14-3-3ζnoW) and the C-terminally truncated 14-3-3ζΔC (residues 1–230 with deleted disordered C-terminal loop) were prepared as described previously (17, 18).

Dynamic Light Scattering (DLS)—DLS measurements were carried out as described previously (15). All measurements were performed in a buffer containing 20 mM Tris-HCl (pH 7.5), 200 mM NaCl, 1 mM EDTA, and 2 mM DTT. The full-length Pdc, Pdc-ND, and Pdc-CD concentrations were 60 μM.

Circular Dichroism (CD) Spectroscopy—Both far- and near-UV CD spectra were measured as described previously (19). The CD measurements were conducted at 22 °C in a buffer containing 20 mM Tris-HCl (pH 7.5), 200 mM NaCl, 1 mM EDTA, and 2 mM 2-mercaptoethanol with protein concentrations of 10 μM (far-UV spectra) and 80–160 μM (near-UV spectra).

Analytical Ultracentrifugation (AUC)—Sedimentation velocity (SV) experiments were performed using a ProteomeLab™ XL-I analytical ultracentrifuge (Beckman Coulter) as described previously (19). Samples were dialyzed against buffer containing 20 mM Tris-HCl (pH 7.5), 200 mM NaCl, and 2 mM 2-mercaptoethanol before analysis. All sedimentation profiles were recorded with absorption optics. The diffusion-deconvoluted sedimentation coefficient distributions $c(s)$ were calculated from raw absorbance data using the software package SEDFIT (20). SV analysis of interaction between full-length pPdc (pPdc-ND and Pdc-CD) and 14-3-3ζΔC was performed at various loading concentrations and molar ratios; this was followed by the integration of calculated distributions to determine the overall weight-averaged s values (s_w). Constructed s_w isotherms were fitted with $A + B \rightleftharpoons AB$ model as implemented in the software package SEDPHAT with known s_w values of individual components as prior knowledge. Resulting parameters were verified, and loading concentrations were corrected using the global Lamm equation modeling also implemented in the SEDPHAT software (20, 21).

Small Angle X-ray Scattering—SAXS data were collected on the European Molecular Biology Laboratory (EMBL) P12 beamline on the storage ring PETRA III (Deutsches Elektronen Synchrotron (DESY), Hamburg, Germany). The SAXS measurements were conducted in buffer containing 20 mM Tris-HCl (pH 7.5), 200 mM NaCl, 1 mM EDTA, and 2 mM 2-mercaptoethanol. The Pdc concentrations were 2.3, 3.4, and 4.2 $mg \cdot ml^{-1}$. The data were averaged, and the scattering of buffer was subtracted using PRIMUS (22). The forward scattering $I(0)$ and the radius of gyration R_g were calculated using the Guinier approximation (23). The distance distribution functions $P(r)$ and the maximum particle dimensions D_{max} were computed from the entire scattering pattern using the program GNOM (24). The solute apparent molecular mass (MM_{exp}) was estimated by comparison of the forward scattering with that from reference solutions of bovine serum albumin (molecular mass 66 kDa). *Ab initio* molecular envelopes were computed by the program DAMMIN (25). Multiple iterations of DAMMIN were aver-

aged using the program DAMAVER (26). The analysis based on the ensemble optimization method was performed using the program EOM (27).

Time-resolved Fluorescence Measurements—Fluorescence decays were measured on an apparatus described previously (28). The apparatus included frequency-tripled Ti:Sapphire laser (Coherent, Chameleon Ultra II) and the time-correlated single photon counting detection (Becker&Hickl, SPC150) with cooled MCP-PMT (Hamamatsu, R3809U-50). Tryptophan was excited at 298 nm, and its emission was collected at 355 nm using a monochromator (Horiba, H-20) with a stack of UG1 and BG40 glass filters placed in front of the input slit. ANS emission was excited and measured at 355 and 480 nm, respectively, using the monochromator with the 405-nm long-pass filter in the emission channel. Decays were accumulated under the magic angle conditions, typically in 1024 channels and a time resolution of 50 ps/channel, until 10^7 counts per decay were reached. Samples were placed in a thermostatic holder, and all experiments were performed at 23 °C in a buffer containing 20 mM Tris-HCl (pH 7.5), 200 mM NaCl, 1 mM EDTA, and 2 mM 2-mercaptoethanol. The Pdc concentration was 30 μM, and the 14-3-3ζnoW protein concentration was 60 μM. ANS fluorescence experiments were performed with 5 μM Pdc and 20 μM ANS. Fluorescence was assumed to decay multiexponentially according to Equation 1,

$$I(t) = \sum_i \alpha_i \cdot \exp(-t/\tau_i) \quad \text{(Eq. 1)}$$

where $32\ \Sigma_i\ \alpha_i = 1$ and τ_i and α_i are the fluorescence lifetimes and the corresponding amplitudes, respectively. Decays were analyzed by a singular value decomposition maximum entropy method for oversampled data (29). The program yields amplitudes, α_i, representing lifetime distributions. Typically, we used 100 lifetimes equidistantly spaced in the logarithmic scale, ranging from 50 ps to 100 ns. The mean fluorescence lifetime of the whole decay was calculated from Equation 2,

$$\tau_{\text{mean}} = \sum_i \alpha_i \tau_i^2 / \sum_i \alpha_i \tau_i \quad \text{(Eq. 2)}$$

Polarized fluorescence decays were measured with fixed emission polarizer set in the vertical position, and the excitation polarization plane was rotated between 0 and 90°. In this configuration the G-factor was close to one, and its value was determined in an independent experiment. Fluorescence anisotropy decays $r(t)$ were obtained by simultaneous reconvolution of parallel $I_{\parallel}(t)$ and perpendicular $I_{\perp}(t)$ decay components (30, 31) using model-independent singular value decomposition maximum entropy method that does not set prior limits on the distribution shape (29). The anisotropies $r(t)$ were assumed to decay multiexponentially as shown in Equation 3,

$$r(t) = \sum_i \beta_i' \cdot \exp(-t/\phi_i') \quad \text{(Eq. 3)}$$

where amplitudes β'_i represent a distribution of the correlation times ϕ'_I ($\Sigma\beta'_i = r_0$), and r_0 is the initial anisotropy. We used 100 correlation times ϕ'_i equidistantly spaced in the logarithmic scale and ranging from 50 ps to 200 ns. For multimodal distributions, the mean correlation time associated with the m-th peak of the distribution was calculated from Equation 4,

$$\phi_m = \sum_k \beta'_{m,k} \cdot \phi'_{m,k} / \sum_k \beta'_{m,k} \quad \text{(Eq. 4)}$$

where index k runs over the nonzero amplitudes of the m-th peak of the distribution only. The area of the peak represents the associated mean amplitude β_m.

Tryptophan Fluorescence Quenching Experiments—Fluorescence quenching measurements were performed at 22 °C on an ISS PC1 photon counting spectrofluorometer, using a 1-nm bandpass on both the excitation and emission monochromators. Samples (35 μM pPdc and 70 μM 14-3-3ζnoW) were dialyzed against buffer containing 20 mM Tris-HCl (pH 7.5), 200 mM NaCl, 1 mM EDTA, and 2 mM 2-mercaptoethanol. Stern-Volmer plots were constructed using the changes in fluorescence intensity at 340 nm (with excitation at 297 nm) and fitted with Equation 5,

$$I_0/I = (1 + K_{SV}[Q])e^{V[Q]} \quad \text{(Eq. 5)}$$

where I_0 is the fluorescence intensity in the absence of the quencher; I is the fluorescence intensity of the sample in the presence of the quencher with the concentration $[Q]$; K_{SV} is the Stern-Volmer constant, and V is the static quenching constant. The K_{SV} is equal to $\tau_{\text{mean}}\ k_q$, where k_q is the bimolecular rate constant for quenching, and τ_{mean} is a mean fluorescence lifetime of the tryptophan in the absence of a quencher (32). Corrections for the inner filter effect were performed as described previously according Equation 6 (33),

$$I_c = I\ \text{antilog}((A_{ex} + A_{em})/2) \quad \text{(Eq. 6)}$$

where I_C is the corrected fluorescence intensity; I is the measured fluorescence intensity, and A_{ex} and A_{em} are sample absorbances at the excitation and emission wavelength, respectively.

Hydrogen-Deuterium Exchange Kinetics Coupled to Mass Spectrometry—Hydrogen/deuterium exchange was followed for individual proteins alone (Pdc, pPdc, and 14-3-3ζΔC) and for 2:1 molar mixture of 14-3-3ζΔC:pPdc. Concentrations of the proteins during exchange were 120 μM for 14-3-3ζΔC and 60 μM for Pdc or pPdc. HDX was started by a 5-fold dilution of the proteins to deuterated buffer (20 mM Tris-HCl, pD 7.5, 200 mM NaCl, 1 mM EDTA, 5 mM DTT, 10% glycerol), and aliquots of 10 μl were collected at 40 s, 4 and 15 min, and 1, 3, and 8 h of exchange. Exchange was stopped by the addition of 57 μl of 6 mM HCl and freezing in liquid nitrogen. Analysis of deuterated samples (HPLC-MS) and data processing were done as described elsewhere (34) except for the following modifications. Injection volume was 20 μl and shorter gradient was used, 10–25% B (95% acetonitrile, 5% water, 0.4% formic acid) in 5 min, followed by a quick step to 40% B.

Results

N-terminal Domain of Pdc Is Intrinsically Disordered Protein and Adopts Highly Extended Conformation—The crystal structure of the Pdc·$G_t\beta\gamma$ complex revealed that Pdc-ND includes the first 110 amino acid residues (Fig. 1*A*) and constitutes the main part of Pdc's interaction surface with $G_t\beta\gamma$ (13, 35). It has

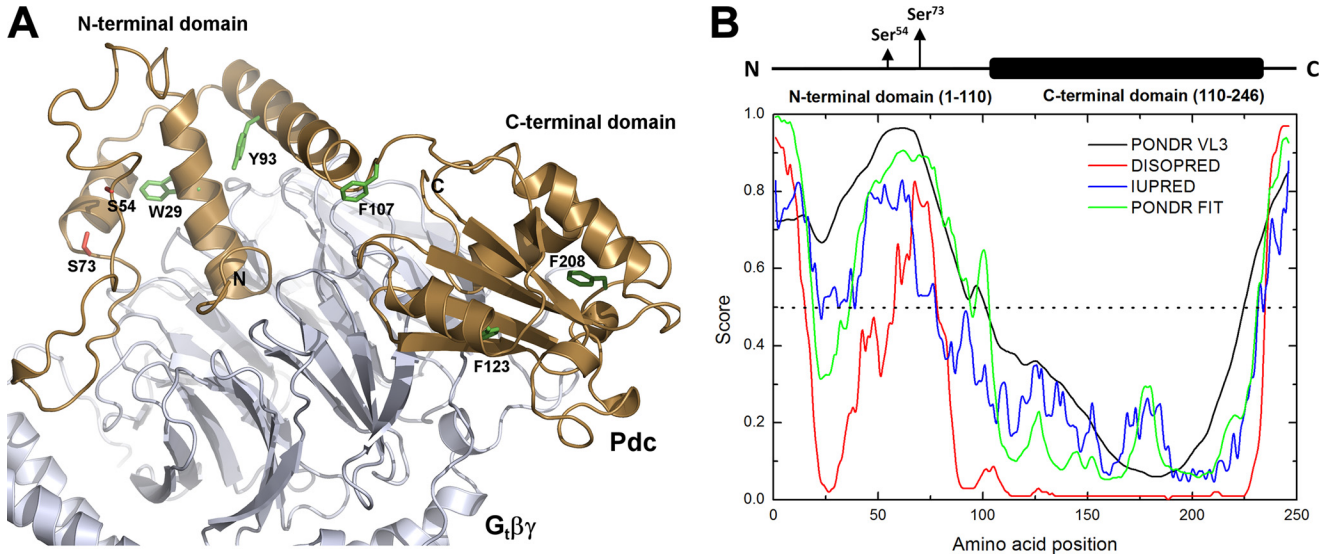

FIGURE 1. **N-terminal domain of unbound (apo) Pdc is inherently disordered.** *A,* crystal structure of the Pdc·$G_t\beta\gamma$ complex (13). The $G_t\beta\gamma$ complex and Pdc are shown in *gray* and *light brown*, respectively. Phosphorylation sites Ser^{54} and Ser^{73} are shown in *red*. Residues that were mutated to prepare single Trp-containing mutants of Pdc are shown in *green*. *B,* bioinformatics analysis using PONDR VL3 (36), DISOPRED (37), UIPRED (38), and PONDR FIT (39) predictors suggests that the majority of Pdc-ND (residues 1–101) and the very C terminus of Pdc-CD (residues 225–246) are unstructured. The position of both phosphorylation sites/the 14-3-3 protein-binding motifs is shown on *top*.

also been suggested that this domain is poorly structured in the apo-state compared with the ordered and helical conformation observed in the complex with $G_t\beta\gamma$ (14). Because both regulatory phosphorylation sites and the 14-3-3 protein-binding motifs (Ser^{54} and Ser^{73}) are located within this presumably unstructured Pdc-ND, we first performed its detailed biophysical characterization using DLS, analytical ultracentrifugation, and fluorescence spectroscopy. The analysis of Pdc sequence using PONDR VL3 (36), DISOPRED (37), UIPRED (38), and PONDR FIT (39) predictors suggests that the majority of Pdc-ND (residues 1–101) and the very C terminus of Pdc-CD (residues 225–246) are unstructured (Fig. 1*B*). Another typical feature of unstructured proteins is their low compactness. Thus, DLS measurements were performed to obtain information on the hydrodynamic radii (R_H) of Pdc and its isolated domains. The comparison of R_H reveals that Pdc-ND, although possessing a smaller number of amino acid residues compared with Pdc-CD, exhibits significantly larger R_H (Table 1). Both full-length Pdc and Pdc-ND also show significantly larger R_H compared with theoretical values calculated for proteins of given molecular masses in a natively folded state (Table 1) (40). In addition, the experimental R_H of Pdc-ND is comparable with the theoretical value calculated for its guanidinium chloride-unfolded state supporting the disordered nature of this domain.

The SV AUC experiments were next performed to confirm that large values of R_H observed for Pdc and Pdc-ND were due to a nonglobular structure and not their oligomerization. The normalized continuous sedimentation coefficient distributions, $c(s)$, obtained from these experiments, are shown in Fig. 2*A*. The analysis of distributions reveals that Pdc-ND, Pdc-CD, and full-length Pdc shows single peaks with a weight-averaged sedimentation coefficient (corrected to 20.0 °C and the density of water), $s_{w(20,\,w)}$, values of 1.5, 1.8, and 2.4 S, respectively. These values of $s_{w(20,\,w)}$ correspond to molecular masses of

TABLE 1
Biophysical properties of Pdc full-length, Pdc-ND and Pdc-CD

	Pdc full-length	Pdc-ND	Pdc-CD
No. of residues[a]	265	126	156
Theoretical molecular mass[b] (g/mol)	30161.4	14643.2	17414.2
Experimental R_H from DLS[c] (Å)	38.4 ± 0.5	35.4 ± 0.4	26.0 ± 0.1
Theoretical R_H[d] (Å), natively folded	24.8	19.2	20.4
Theoretical R_H[d] (Å), MG	27.7	21.8	23.1
Theoretical R_H[d] (Å), NU coil	45.4	31.8	34.7
Theoretical R_H[d] (Å), NU PMG	36.8	27.5	29.5
Theoretical R_H[d] (Å, Gdm-Cl-unfolded	51.2	34.6	38
$s_{w(20,\,w)}$[e] (S)	2.4	1.5	1.8
τ_{mean} of ANS[f,g] (ns)	7.4	3.7	5.7

[a] This includes the N-terminal His_6 tag.
[b] Data were calculated from the sequence.
[c] Values are the mean ± S.D. of five measurements.
[d] Theoretical values of R_H for various conformational states were calculated according to equations reported by Uversky (40). MG is molten globule state; NU coil is natively unfolded state behaving as random coil; NU PMG is more compact natively unfolded state resembling premolten globule state; GdmCl-unfolded is unfolded state in the presence of guanidinium chloride.
[e] Weight-averaged sedimentation coefficient was corrected to 20.0 °C, and the density of water was obtained from analytical ultracentrifugation.
[f] S.D. = 0.05 ns.
[g] The mean fluorescence lifetime (τ_{mean}) was calculated using Equation 2.

~14.4, ~18.7, and ~31.8 kDa, respectively, suggesting all three proteins are monomers in solution (theoretical molecular mass of Pdc-ND, Pdc-CD, and full-length Pdc are 14.64, 17.41, and 30.16 kDa, respectively).

The disordered nature of Pdc-ND is also corroborated by its CD spectra. The far-UV CD spectrum shows a large negative ellipticity in the region around 200 nm similarly to spectra of other intrinsically disordered proteins including the *Listeria monocytogenes* virulence protein ActA (41), the bovine viral diarrhea virus core protein (42), or the substrate domain of $p130^{Cas}$ (Fig. 2*B*) (43). In addition, the near-UV CD spectrum of Pdc-ND is weak and featureless, suggesting its aromatic side chains have no well defined conformation, thus corroborating the disordered state of this domain (Fig. 2*C*). In contrast, the CD spectra of Pdc-CD show features of a well folded protein containing a significant amount of secondary structure and

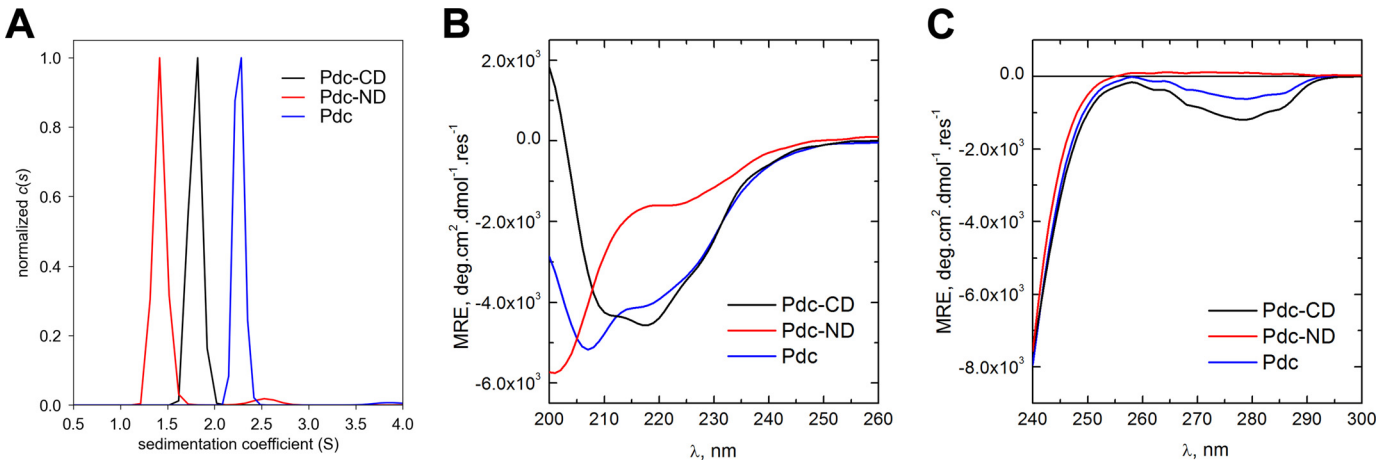

FIGURE 2. **Biophysical characterization of Pdc domains.** *A*, normalized continuous distribution of sedimentation coefficients, *c*(*s*), for Pdc full-length, Pdc-CD, and Pdc-ND. *B*, comparison of the far-UV CD spectra of Pdc full-length, Pdc-CD, and Pdc-ND. *C*, comparison of the near-UV CD spectra of Pdc full-length, Pdc-CD, and Pdc-ND.

whose aromatic side chains possess a well defined conformation (44).

The structural differences between Pdc-ND and Pdc-CD were next studied using time-resolved fluorescence of ANS. It has been shown that this hydrophobic fluorescence probe has significantly higher affinity for folded and partly folded proteins than for the unstructured and/or unfolded ones, and thus it is frequently used to study structural properties of protein molecules (45). The ANS binding to and/or into hydrophobic regions of folded or molten globular proteins is accompanied by the characteristic increase in the mean excited-state lifetime (τ_{mean}). The measured values of τ_{mean} of ANS bound to Pdc, Pdc-ND, and Pdc-CD are shown in Table 1. The significantly lower value of τ_{mean} for ANS bound to Pdc-ND compared with Pdc-CD or Pdc is consistent with the expected unfolded state and the low hydrophobicity of the N-terminal domain. Thus, all these data suggest that Pdc-ND is intrinsically disordered and adopts a highly extended conformation.

Solution Structure of the Free Pdc—Because the unbound (apo) structure of Pdc is unknown, we next used the SAXS, an established technique for structural analysis of flexible systems, including intrinsically disordered proteins (46), to study the solution structure of Pdc. The Guinier analysis revealed that all Pdc samples are monodisperse as their Guinier plots are linear in the region $s^*R_g < 1.3$, where *s* is the momentum transfer, and R_g is the radius of gyration (Fig. 3*A*). Values of the R_g calculated from the slope of the Guinier plot (R_g = 36.5–37.0 Å) suggest that the free Pdc adopts an extended state (Table 2). In comparison, the globular molecule of the 14-3-3 protein dimer (yeast isoform Bmh1) with double molecular weight has a R_g value of 32.6 Å (47). The distance distribution functions *P*(*r*) calculated from the scattering data using the program GNOM (24) are shown in Fig. 3*B*. The *P*(*r*) functions are similarly shaped for all measured Pdc samples and show peak around 27 Å and the maximum distance D_{max} 120–129 Å (Table 2). The elongated and highly asymmetric shape of the *P*(*r*) functions corroborates the extended state of the Pdc molecule. The calculated molecular weight derived from the forward scattering intensity *I*(0) is consistent with the expected molecular weight of the Pdc monomer (Table 2). The Kratky plot ($s^2I(s)$ *versus s*), which reflects the degree of compactness of the scattering particles, has a shape typical for a partially unfolded protein with flat peak at low *s* and an increase in $s^2I(s)$ in the larger *s* range (Fig. 3*C*) (48, 49).

Two different approaches were used to model the solution structure of free Pdc. First, the low resolution *ab initio* envelope of Pdc was calculated using DAMMIN (25). The final envelope consists of an average of 10 individual reconstructions and the individual envelopes agreed well with each other (the mean value of normalized spatial discrepancy was 0.52 ± 0.03). The obtained *ab initio* envelope of Pdc possesses a rod-like extended shape with one end being narrower than the other (Fig. 3*D*). The size of the narrower smaller part corresponds well with the size of Pdc-CD, suggesting that the larger and wider part represents the disordered N-terminal domain. However, the validity of such *ab initio* reconstruction for disordered proteins, which describes a highly flexible structure using one conformation, is uncertain although useful to visualize a diffuse nature of disordered molecule (46, 50). Therefore, we next used a more appropriate approach based on the EOM (27). The C-terminal domain of Pdc (residues 106–230) was treated as a rigid body and the flexible N-terminal domain and the very C terminus (residues 1–105 and 231–246, respectively) as a chain of dummy residues. An initial pool of 10,000 Pdc models with random conformation of the N-terminal domain and the very C terminus free of steric clashes was generated. Next, a genetic algorithm was used to select an ensemble of Pdc conformers that collectively fit the experimental SAXS data. The EOM analysis yielded an ensemble (containing 18 conformers) that fits the experimental scattering curve of Pdc (*c* = 4.2 mg/ml) with χ^2 value of 0.98 (Fig. 4*A*). The comparison of the R_g distributions of the EOM-selected conformational ensemble with the initial pool is shown in Fig. 4*B*. As can be noticed, the R_g distribution of the EOM-selected ensemble is narrower and biased toward less compact structures when compared with the pool, and it contains single peak centered around an R_g of 34.2 Å, consistent with R_g values calculated from the scattering curves (Table 2). Very similar results were also obtained from the EOM analysis of other two Pdc samples (*c* = 3.4 and 2.3 mg/ml). The selected conformers that fit the experimental scat-

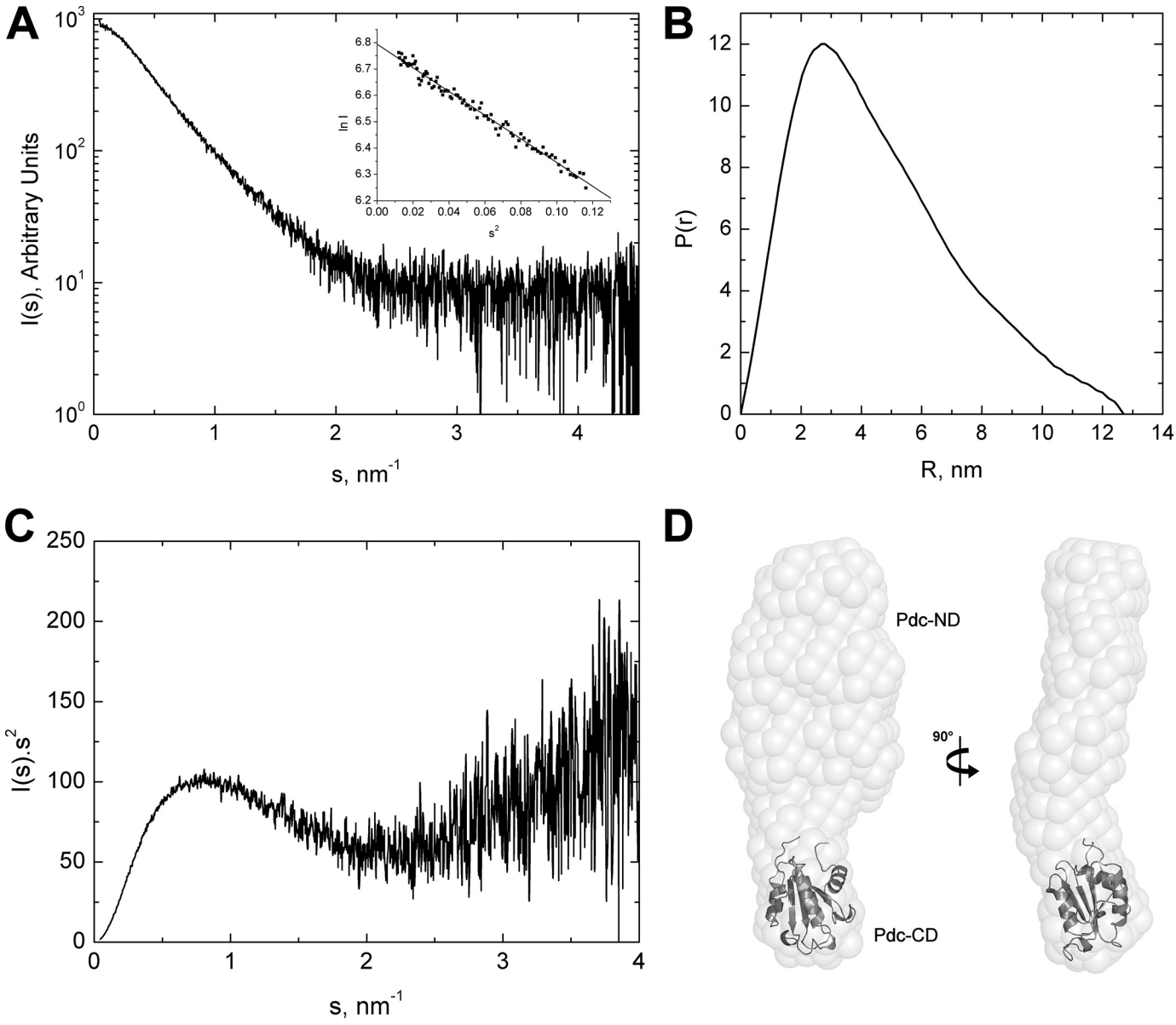

FIGURE 3. **Structural characterization of Pdc by SAXS.** *A,* scattering intensity as a function of the scattering vector s ($s = 4\pi\sin(\theta)/\lambda$, where 2θ is the scattering angle, and λ is the wavelength). *Inset* shows Gunier plot of Pdc at concentration 4.2 mg/ml. *B,* distance distribution function $P(r)$. *C,* Kratky plot, which reflects the degree of compactness of the scattering particles, has a shape typical for a partially unfolded protein with flat peak at low s and an increase in $s^2I(s)$ in the larger s range (48, 49). *D,* averaged and filtered DAMMIN shape envelope of Pdc molecule. The size of the narrower smaller part corresponds well with the size of Pdc-CD, suggesting that the larger and wider part represents the disordered N-terminal domain.

TABLE 2
Structural parameters determined from SAXS data

	Pdc sample		
c (mg·ml^{-1})	4.2	3.4	2.3
R_g (Å)[a]	36.6 ± 0.3	37.0 ± 0.3	36.5 ± 0.4
R_g (Å)[b]	37.2 ± 0.3	37.9 ± 0.2	36.2 ± 0.3
D_{max} (Å)	127	129	120
MM_{exp} (kDa)[c]	33 ± 1	34 ± 1	33 ± 1

[a] Data were calculated using Guinier approximation (23).
[b] Data were calculated using the program GNOM (24).
[c] Molecular weight was estimated by comparison of the forward scattering intensity $I(0)$ with that from the reference solution of bovine serum albumin.

tering curve with the lowest χ^2 value (Fig. 4*C*) show substantial structural variability (the mean value of normalized spatial discrepancy is 2.02), suggesting significant flexibility of the N-terminal domain. In addition, none of these conformers by itself could account for the observed Pdc scattering, as revealed by comparing the $P(r)$ curves calculated from these models with the experimental $P(r)$ curve (Fig. 4*D*). We also attempted to model the Pdc molecule as two rigid domains connected with the flexible linker similarly to Pdc structure observed in the Pdc·$G_t\beta\gamma$ complex (13, 14). However, the EOM analysis using this model yielded an ensemble that fits the experimental scattering curve of Pdc significantly worse (with χ^2 value of 1.51) compared with the model containing ordered C-terminal domain and disordered N-terminal domain (Fig. 4*E*). In addition, the comparison of the R_g distributions of the EOM-selected ensemble with the pool revealed that the molecule of Pdc is significantly more extended than expected from the pool simulation (Fig. 4*F*), indicating that the two-domain model is unable to properly describe the solution structure of free Pdc.

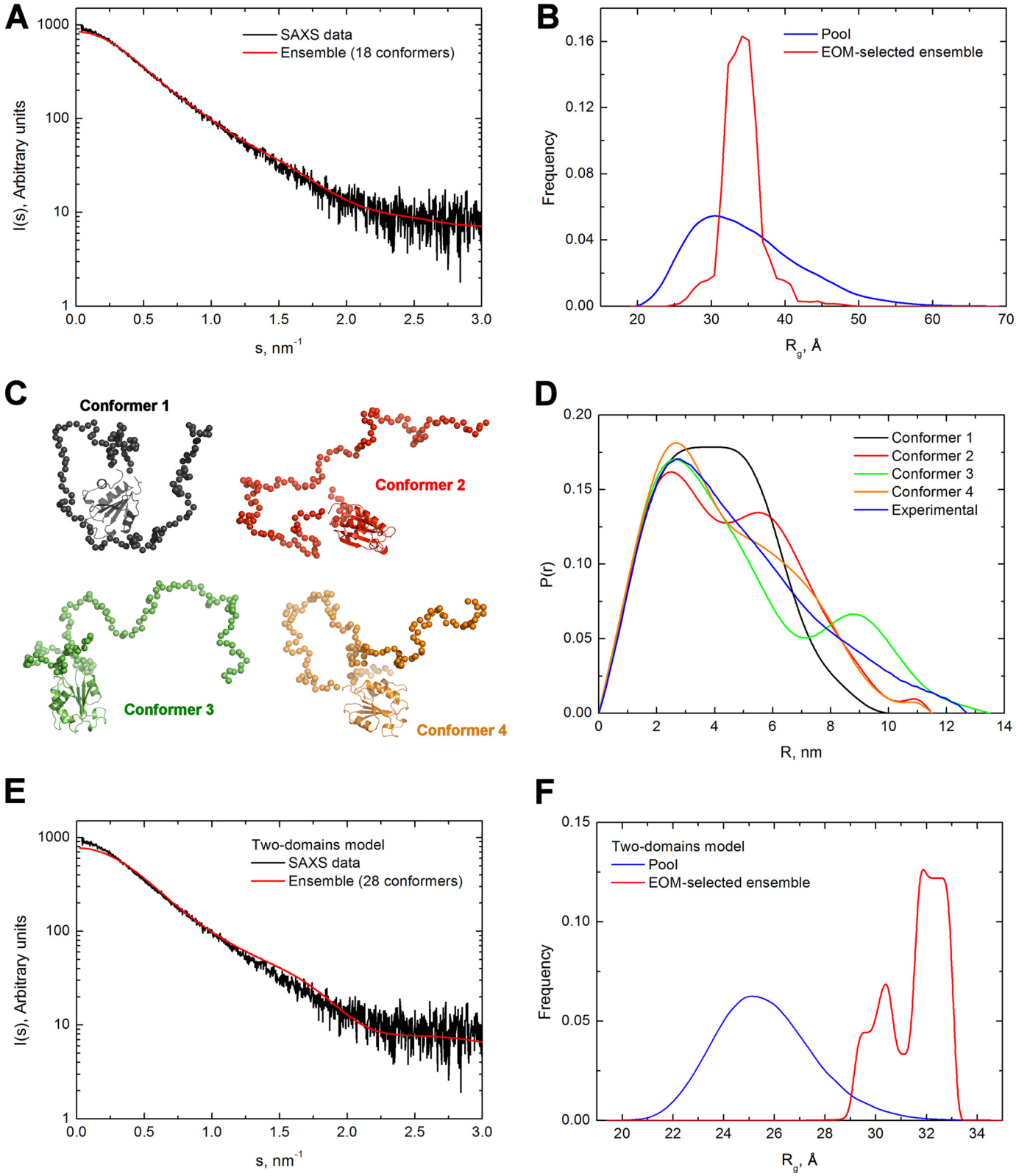

FIGURE 4. **EOM analysis of Pdc SAXS data.** *A,* comparison of the experimental SAXS profile (shown in *black*) with the theoretical one (shown in *red*) derived from an ensemble calculated using the EOM with the Pdc model based on flexible Pdc-ND and folded Pdc-CD. The selected ensemble fits the experimental scattering curve of Pdc with $\chi^2 = 0.98$. *B,* comparison of the R_g distributions of the EOM-selected conformational ensemble (shown in *red*) with the initial pool (shown in *blue*) calculated from the model with the flexible Pdc-ND. *C,* EOM-generated models of Pdc that fit the experimental scattering curve with the lowest χ^2 value. Residues from flexible parts of Pdc molecule are represented by *spheres*. *D,* comparison of the *P*(*r*) curves calculated from EOM-generated models (shown in *black*, *red*, *green,* and *orange*) with the experimental *P*(*r*) curve (shown in *blue*). As can be noticed, none of these conformers by itself could account for the observed Pdc scattering. *E,* comparison of the experimental SAXS profile (shown in *black*) with the theoretical one (shown in *red*) derived from an ensemble calculated using the EOM with the Pdc model consisting of two rigid domains. The selected ensemble fits the experimental scattering curve of Pdc with $\chi^2 = 1.51$. *F,* comparison of the R_g distributions of the EOM-selected ensemble with the initial pool calculated from the Pdc model consisting of two rigid domains.

TABLE 3
Summary of time-resolved tryptophan fluorescence measurements of Pdc

Pdc mutant	τ_{mean} [a,b]	β_1 [b]	ϕ_1 [c]	β_2 [c]	ϕ_2 [d]	β_3 [c]	ϕ_3 [d]
	ns		*ns*		*ns*		*ns*
Pdc Trp^{29}	3.9	0.045	0.5	0.094	2.4	0.061	36
pPdc Trp^{29}	3.8	0.057	0.4	0.102	2.7	0.043	36
pPdc Trp^{29} + 14-3-3ζ[e]	4.2	0.028	0.4	0.067	1.8	0.108	71
Pdc Trp^{93}	4.3	0.065	0.6	0.048	3.2	0.086	22
pPdc Trp^{93}	4.1	0.055	0.9	0.050	3.0	0.091	23
pPdc W93P + 14-3-3ζ	4.4	0.022	0.3	0.044	1.8	0.137	51
Pdc Trp^{107}	4.9	0.034	0.3	0.045	1.6	0.122	33
pPdc Trp^{107}	4.9	0.035	0.4	0.043	1.9	0.120	34
pPdc Trp^{107} + 14-3-3ζ	5.0	0.029	0.8	0.036	1.5	0.137	54
Pdc Trp^{123}	4.5	0.036	0.6			0.160	20
pPdc Trp^{123}	4.3	0.031	0.4			0.170	20
pPdc Trp^{123} + 14-3-3ζ	4.3	0.017	0.4	0.019	1.4	0.166	32
Pdc Trp^{208}	4.6	0.081	0.6			0.116	15
pPdc Trp^{208}	4.2	0.074	0.5			0.124	16
pPdc Trp^{208} + 14-3-3ζ	4.4	0.047	0.8	0.013	2.2	0.142	36

[a] S.D. < 0.05 ns.
[b] The mean fluorescence lifetime (τ_{mean}) was calculated using Equation 2.
[c] S.D. < 0.01.
[d] S.D. < 20%.
[e] The human 14-3-3ζnoW protein mutant missing all Trp residues (mutations W59F and W228F) was used in all Pdc tryptophan measurements (17, 51).

Thus, the analysis of SAXS measurements suggests that molecules of free Pdc are monomers that possess extended conformations due to the highly flexible and unstructured N-terminal domain, in agreement with data obtained from DLS, analytical ultracentrifugation, CD spectroscopy, and ANS fluorescence (Table 1 and Figs. 1 and 2).

Conformational Behavior of Pdc and Its Changes upon Phosphorylation and 14-3-3ζ Binding—The time-resolved tryptophan fluorescence intensity and anisotropy decay measurements were next used to investigate the conformational behavior of Pdc and its changes upon phosphorylation and 14-3-3ζ binding. Four Pdc mutants containing a single tryptophan residue at four different positions (Trp^{93}, Trp^{107}, Trp^{123}, and Trp^{208}) were prepared to sample various regions of the Pdc molecule. Residues Trp^{93} and Trp^{107} are located within Pdc-ND and Trp^{123} and Trp^{208} within Pdc-CD (Fig. 1*A*). The sequence of Pdc contains only one tryptophan residue at position 29; thus, this residue was mutated to Phe, and tryptophan was inserted into selected positions (mutations Y93W, F107W, F123W, and F208W). The human 14-3-3ζnoW protein mutant missing all Trp residues (mutations W59F and W228F) was used in all tryptophan fluorescence measurements. We previously showed that these two mutations have no effect on the binding properties of the 14-3-3ζ protein (17, 51). Time-resolved fluorescence intensity and anisotropy decays were analyzed using a singular value decomposition maximum entropy method as described previously (29). Because the tryptophan residue frequently exhibits complicated multiexponential decays whose detailed interpretation is often impossible (52, 53), we decided to use a mean fluorescence lifetime (τ_{mean}) as a robust qualitative indicator of changes in the microenvironments of inserted Trp residues (Table 3 and Fig. 5). For the sake of comparison, this table also contains previously obtained data for residue Trp^{29} (15). As can be noticed, phosphorylation by itself decreased τ_{mean} of Trp^{93}, Trp^{123}, and Trp^{208}, with the effect being surprisingly the strongest for Trp^{208} (Fig. 5*A*). The reduced τ_{mean} can be interpreted as increased contacts with the polar environment and/or altered quenching interactions in the vicinity of these residues, suggesting that in the apo-state both domains interact with each other, and the phosphorylation of Ser^{54} and Ser^{73} within Pdc-ND affects this interaction. However, the interaction between pPdc and 14-3-3ζnoW significantly increased the τ_{mean} of Trp^{29}, Trp^{93}, and Trp^{208} (Fig. 5*B*). This could be the result of either the 14-3-3-induced conformational change of pPdc, which affects interaction of these residues with their surroundings, and/or a direct interaction of 14-3-3ζnoW with these residues, reducing their contacts with the polar environment or altering quenching interactions in their vicinity.

It is reasonable to assume that such interactions would also affect the mobility and/or the accessibility of these residues. Thus, we next studied segmental motions of inserted tryptophans using the polarized time-resolved emission measurements (Table 3 and Fig. 5). The fluorescence anisotropy decays of all five tryptophans revealed three classes of correlation times. Short correlation times located around 0.3–0.9 ns (β_1) and 1.4–3.0 ns (β_2) reflect the fast local motions of tryptophan residues, and the third correlation time, ϕ_3, likely reflects the rotational diffusion of the whole molecule. Changes in the extent of segmental motion of inserted tryptophans can be judged from the change in the sum of amplitudes of fast anisotropy decay components β_{short} ($\beta_{short} = \beta_1 + \beta_2$) (15). Because $\beta_3 = r_0 - \beta_1 - \beta_2 = r_0 - \beta_{short}$, see Equation 3, where r_0 is a constant (33), it is advantageous to evaluate the internal motion from the change of β_3 because it can be assessed with better accuracy than β_{short}. As seen from Equation 3, lower β_3 indicates larger extent of the internal protein mobility and vice versa. The obtained increase in β_3 revealed that the 14-3-3ζnoW binding substantially decreased segmental motions of Trp^{29} and Trp^{93} from pPdc-ND and, to a lesser extent, Trp^{208} from pPdc-CD (Table 3 and Fig. 5*B*). These changes suggest suppressed segmental flexibility of regions where these Trp residues are located, presumably through direct physical contacts. The phosphorylation by itself significantly affected only the region containing Trp^{29}, which is more flexible upon the modification, whereas the mobility of other tryptophans was not significantly affected (Fig. 5*A*). The suggested steric shielding of several Trp resi-

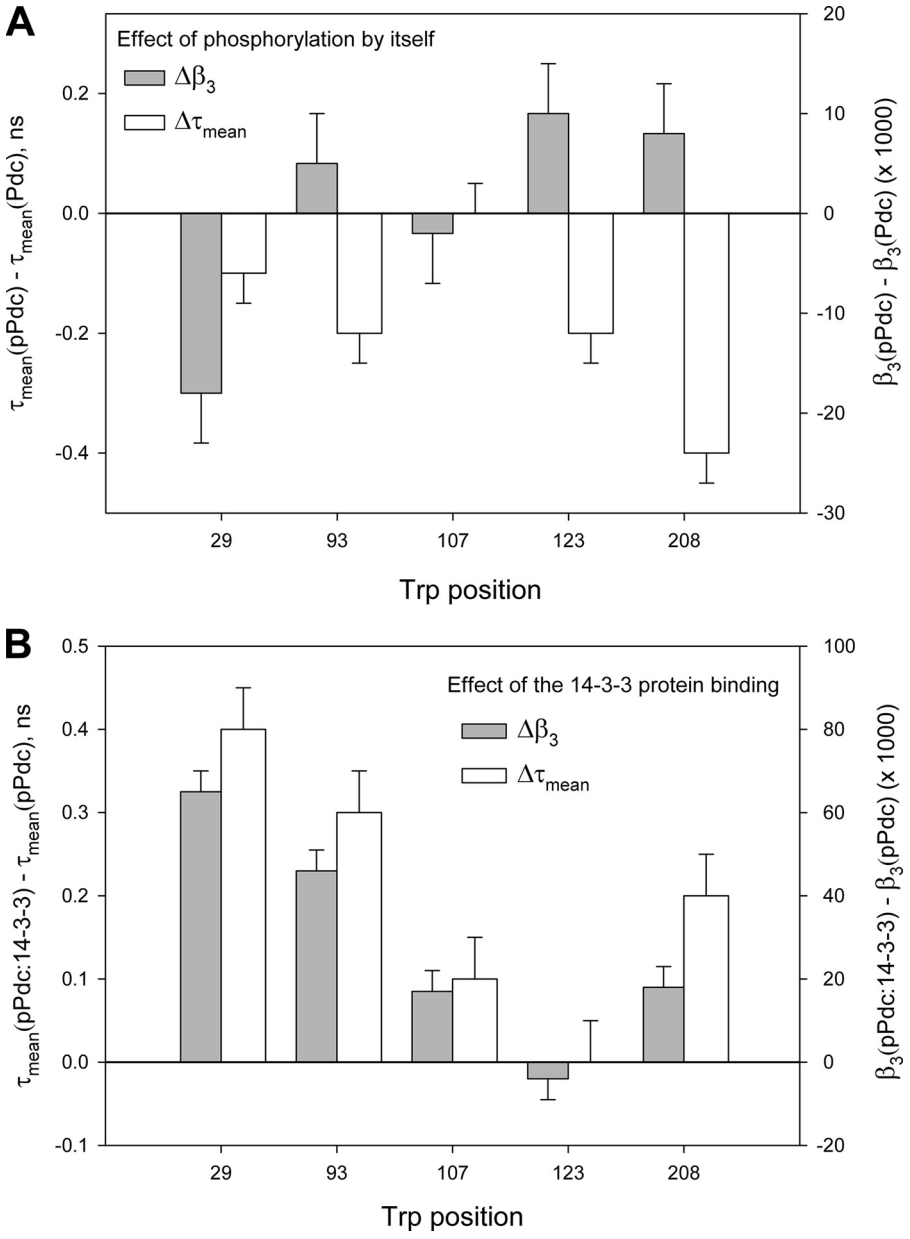

FIGURE 5. **Change in the mean excited-state lifetime, τ_{mean}, and the overall change in amplitudes of slow anisotropy decay component β_3 of Trp^{29}, Trp^{93}, Trp^{107}, Trp^{123}, and Trp^{208}.** *A,* changes induced by phosphorylation of Pdc at Ser^{54} and Ser^{73}. *B,* changes induced by the 14-3-3ζnoW binding to pPdc.

dues by the 14-3-3ζnoW binding should also change their accessibility to the solute quencher. Thus, we next performed acrylamide quenching to test this hypothesis. Table 4 shows values of the bimolecular quenching constant, k_q, that were obtained by fitting the Stern-Volmer plots using Equation 5. As can be noticed, the accessibility of Trp^{29}, Trp^{93}, Trp^{107} and, to a lesser extent, Trp^{208} to the acrylamide significantly decreases in the pPdc·14-3-3ζnoW complex. The accessibility of Trp^{123} to the solvent remains unaltered. In agreement with the fluorescence lifetime data, the quenching experiments indicated for pPdc lower accessibility of Trp^{29}, Trp^{93}, and Trp^{107} from pPdc-ND and Trp^{208} from pPdc-CD in the presence of 14-3-3ζnoW, thus supporting involvement of segments containing these residues in binding to 14-3-3ζ.

TABLE 4
Results of acrylamide quenching of tryptophan fluorescence

Pdc mutant	$k_q \times (10^{-9}\ M^{-1}\ s^{-1})^{a,b}$	V $_{M^{-1}}$
pPdc Trp^{29}	2.08 ± 0.06	0.29 ± 0.05
pPdc Trp^{29} + 14-3-3ζ[c]	1.07 ± 0.03	0.4 ± 0.4
pPdc Trp^{93}	1.12 ± 0.03	0.12 ± 0.06
pPdc Trp^{93} + 14-3-3ζ	0.73 ± 0.05	0.06 ± 0.09
pPdc Trp^{107}	1.35 ± 0.04	0.34 ± 0.09
pPdc Trp^{107} + 14-3-3ζ	0.98 ± 0.08	0.6 ± 0.2
pPdc Trp^{123}	0.63 ± 0.02	0.97 ± 0.04
pPdc Trp^{123} + 14-3-3ζ	0.67 ± 0.02	0.83 ± 0.04
pPdc Trp^{208}	0.43 ± 0.07	
pPdc Trp^{208} + 14-3-3ζ	0.29 ± 0.01	

[a] For comparison, bimolecular quenching constant of Trp in aqueous environment is $k_q = 5.9 \times 10^9\ s^{-1}\ M^{-1}$ (65).
[b] The bimolecular quenching constant (k_q) was calculated using Equation 5.
[c] The human 14-3-3ζnoW protein mutant missing all Trp residues (mutations W59F and W228F) was used in all Pdc tryptophan measurements (17, 51).

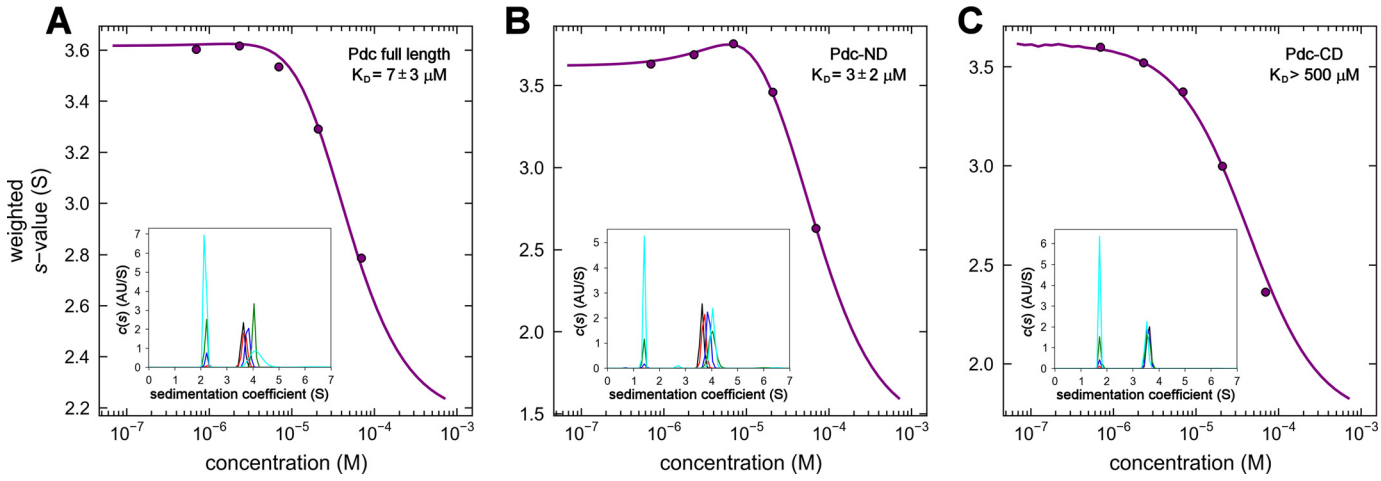

FIGURE 6. **Sedimentation velocity ultracentrifugation.** Isotherms of weight-averaged sedimentation coefficients s_w were obtained from SV AUC experiments using mixtures of 14 μM 14-3-3ζ and 0.7–70 μM full-length pPdc (*A*), pPdc-ND (*B*), and Pdc-CD (*C*). The *insets* show the sedimentation coefficient distributions *c*(*s*) of 14-3-3ζ and pPdc, pPdc-ND, and Pdc-CD mixtures at various molar ratios underlying the s_w data points. Mixtures with the molar ratio 20:1 (14-3-3:Pdc) are shown in *black*, ratio 6:1 in *red*, ratio 2:1 in *blue*, ratio 2:3 in *green*, and ratio 1:5 in *cyan*.

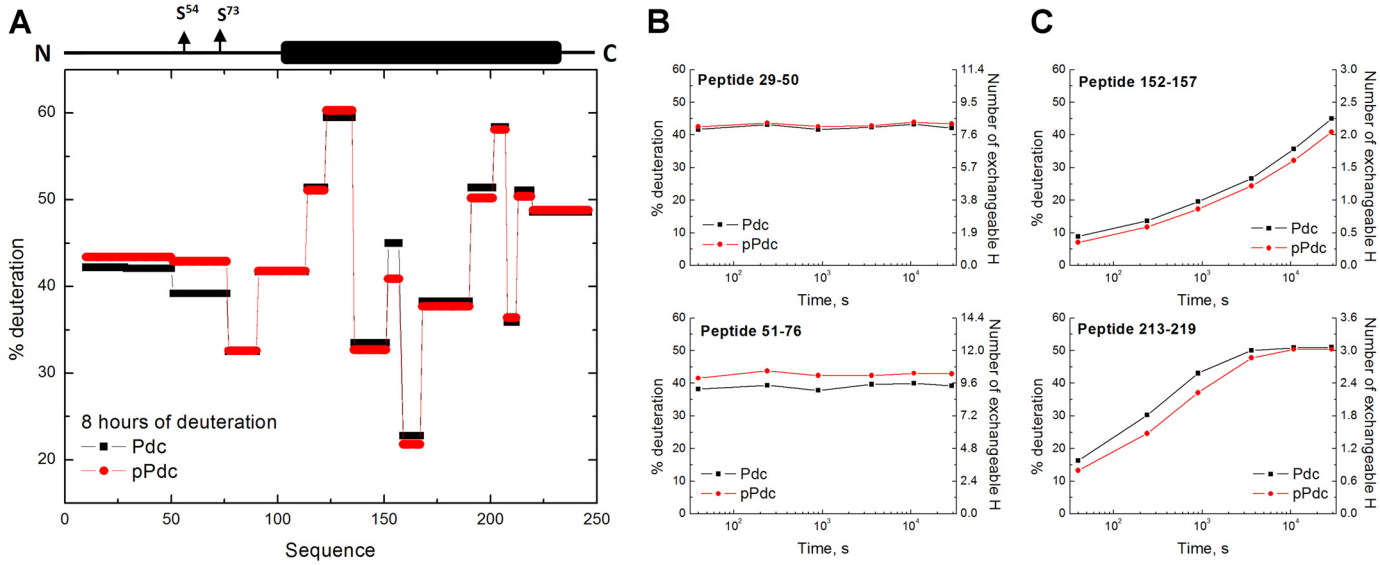

FIGURE 7. **HDX-MS reveals regions of Pdc that are affected by phosphorylation.** *A*, plot showing the deuteration levels of Pdc (shown in *black*) and pPdc (shown in *red*) after 8 h of deuteration. The domain structure of Pdc and the position of both phosphorylation sites/the 14-3-3ζ protein-binding motifs are shown on top. *B*, *graphs* of HDX kinetics for two selected peptides from Pdc-ND. *C*, *graphs* of HDX kinetics for two selected peptides from Pdc-CD. Deuterium exchange is expressed as percentages relative to the maximum theoretical deuteration level (*left vertical axis*) as well as a number of exchangeable protons (*right vertical axis*) for selected Pdc peptide.

Analysis of Interaction between pPdc and 14-3-3ζ Using SV AUC—The AUC was next used to further investigate the interaction between pPdc and 14-3-3ζ. Similarly as in our previous study, we used in these experiments the 14-3-3ζ protein deleted of its C-terminal 15 residues to increase the stability of the pPdc·14-3-3ζ complex (15). This region functions as an autoinhibitor of 14-3-3/ligand interactions and is disordered in all available crystal structures of the 14-3-3 proteins (17, 51, 54). A similar approach was also used by Ottmann *et al.* (55) to stabilize the interaction between 14-3-3 and plant plasma membrane H^+-ATPase. A range of different molar ratios between full-length pPdc (or pPdc-ND and Pdc-CD) and 14-3-3ζ was examined using SV AUC. Analysis of the isotherm of weight-averaged *s* values (s_w isotherm) as a function of pPdc concentration revealed the best fit apparent equilibrium dissociation constant (K_D) of 7 ± 3 μM using a 1:1 (one molecule of pPdc and one 14-3-3ζ dimer) Langmuir binding model (Fig. 6*A*). Interestingly, the analysis of the s_w isotherm determined over a range of different molar ratios between pPdc-ND and 14-3-3ζ revealed that pPdc-ND exhibits slightly higher binding affinity for 14-3-3ζ compared with the full-length pPdc with the best fit K_D of 3 ± 2 μM (Fig. 6*B*). However, the s_w isotherm for Pdc-CD revealed no significant binding interaction with 14-3-3ζ (Fig. 6*C*) suggesting that the phosphorylation-dependent interaction between pPdc-ND and 14-3-3ζ is responsible for the stability of the pPdc·14-3-3ζ complex. In addition, the higher binding affinity observed for pPdc-ND compared with full-length pPdc is consistent with our suggestion that both domains interact with each other (based on results of time-resolved tryptophan fluorescence, Fig. 5*A*), as the removal of Pdc-CD can increase the accessibility of phosphorylated motifs within pPdc-ND.

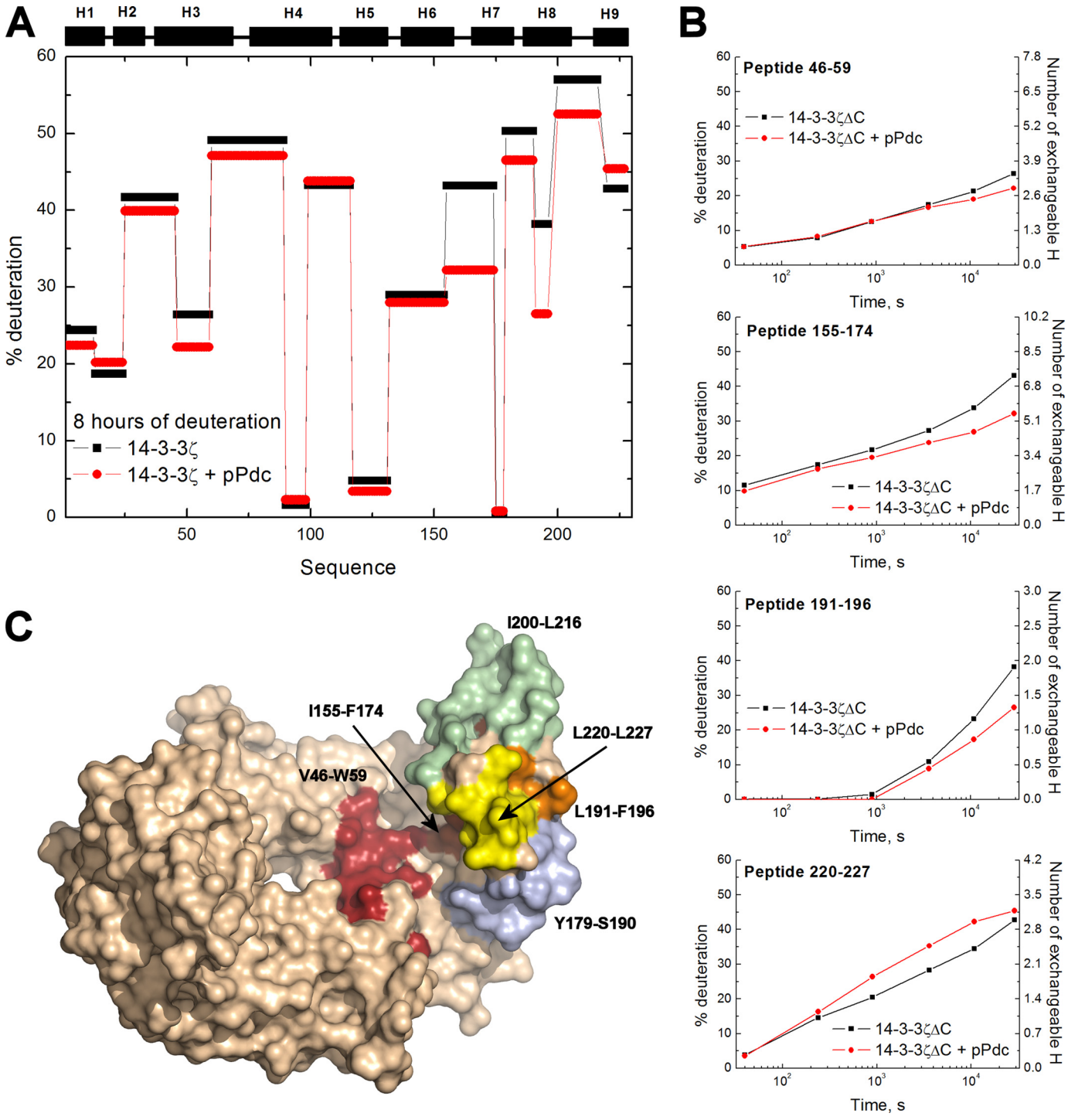

FIGURE 8. **HDX-MS reveals regions of 14-3-3ζ that are affected by pPdc binding.** *A*, plot showing the deuteration levels of 14-3-3ζ in the absence (shown in *black*) and the presence of pPdc (shown in *red*) after 8 h of deuteration. The secondary structure elements of 14-3-3ζ are shown on *top*. *B*, *graphs* representing HDX kinetics for four selected 14-3-3ζ regions that show changed deuterium exchange kinetics upon pPdc binding. Deuterium exchange is expressed as percentages relative to the maximum theoretical deuteration level (*left vertical axis*) as well as a number of exchangeable protons (*right vertical axis*) for selected 14-3-3ζ peptides alone (*black squares*) and in the presence of pPdc (*red circles*). *C*, HDX kinetics for all 14-3-3ζ regions that show changed deuterium exchange kinetics upon pPdc binding (shown in various colors) mapped on the surface representation of the 14-3-3ζ structure (only one chain of the 14-3-3ζ dimer is colored as the changes on the second one are the same) (64).

Mapping of the Interactions between pPdc and 14-3-3ζ Using HDX-MS—Next, HDX-MS was used to map the protein/protein interactions between pPdc and 14-3-3ζ. The HDX kinetics of the complex as well as free 14-3-3ζ, pPdc, and Pdc proteins were measured. The exchange kinetics of 14-3-3ζ was followed on 121 peptides covering 100% of the sequence, although 87 peptides were used in the case of Pdc also covering the entire sequence. The exchange kinetics profile of Pdc alongside the sequence (Fig. 7*A*) revealed that the N-terminal half of the Pdc molecule exhibits relatively fast deuteration kinetics reflecting

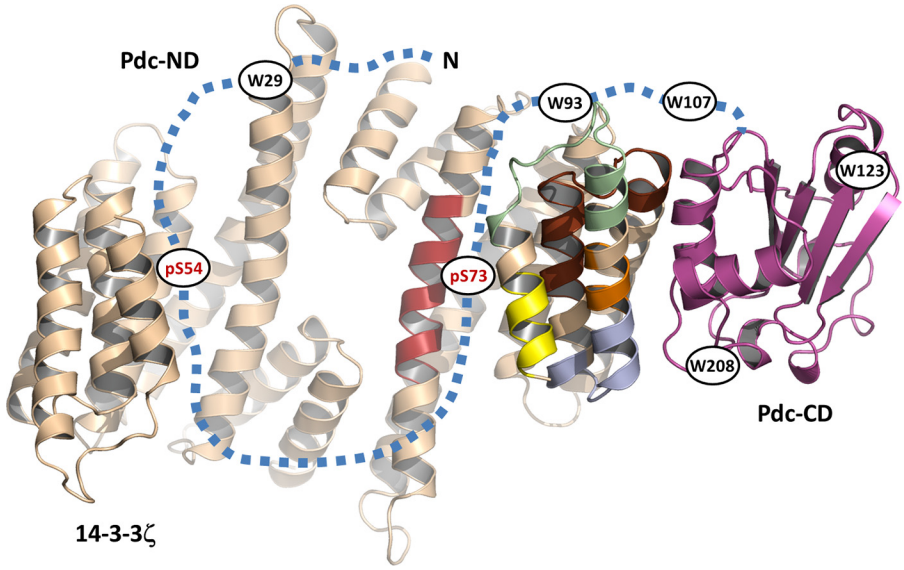

FIGURE 9. **14-3-3ζ protein interacts with and sterically occludes both the N- and C-terminal $G_t\beta\gamma$ binding interfaces of pPdc.** The 14-3-3ζ protein and Pdc-CD are shown in *light brown* and *violet*, respectively. The 14-3-3ζ regions that show changed deuterium exchange kinetics upon pPdc binding are colored as in Fig. 8*C*. The missing Pdc-ND is schematically shown as a *blue dashed line*. The approximate positions of phosphorylation sites Ser^{54} and Ser^{73} as well as tryptophan residues used in quenching and time-resolved fluorescence experiments are also shown. The pPdc·14-3-3ζ complex stoichiometry (1:2) as well as the simultaneous engagement of both ligand binding grooves within the 14-3-3ζ dimer by phosphorylated Ser^{54} and Ser^{73} are based on previously published data (15). As can be seen, the 14-3-3ζ protein binding would sterically occlude the whole Pdc-ND as well as part of Pdc-CD. The position of Pdc-CD is based on results of tryptophan fluorescence measurements (Tables 3 and 4).

its disordered and highly flexible character (Fig. 7*B*), whereas the C-terminal half is characterized by exchange curves typical for structured protein regions (Fig. 7*C*). In general, phosphorylation does not induce differences in solvent accessibility and/or hydrogen bonding except for three regions of the Pdc molecule where significant changes were observed. The first region, around the phosphorylation motif (delimited here by the peptide 51–76), exhibited higher deuteration upon phosphorylation, which can be interpreted as better accessibility of this part of Pdc. In contrast, the second region (peptide 152–157) and the third region (*e.g.* peptide 213–223) show protection of Pdc against deuterium exchange upon phosphorylation. This change in deuteration kinetics is consistent with the existence of contacts between Pdc-CD and Pdc-ND as also suggested by SAXS and time-resolved fluorescence measurements. The HDX for pPdc in the presence of 14-3-3ζ revealed no significant changes in deuteration kinetics considering the errors of the experiment. This insensitivity of pPdc backbone amide hydrogens to changes in deuteration kinetics upon the binding to 14-3-3ζ might be caused either by the highly flexible character of Pdc-ND as such regions undergo a very fast deuteration kinetics that are less sensitive to protein/protein interactions or by the predominantly electrostatic and side chain-mediated interactions between these two proteins. A similar effect was also observed, for example, for phosphorylated RGS3 in the complex with 14-3-3ζ (56) or the heteromeric complex containing UBC9 and SUMO-1 (57). Moreover, several regions of 14-3-3ζ (sequences 46–59, 155–174, and 191–196) exhibited a significant decrease in deuterium incorporation upon the pPdc·14-3-3ζ complex formation (Fig. 8, *A* and *B*). This slower exchange kinetics can be interpreted as lower solvent exposure and/or the change in hydrogen bonding following the binding to pPdc, thus suggesting that protected regions of 14-3-3ζ (or their parts) form the binding interface. Furthermore, as can be noticed from Fig. 8*C*, these regions map not only to the surface of the ligand binding groove formed by helices H3, H5, and H7 but also to the surface formed by helices H6 and H8 outside the central channel similarly as has been observed in the RGS3·14-3-3ζ and the Nth1·Bmh1 complexes (47, 56, 58). Surprisingly, the C-terminal part of helix H9 (peptide 220–227) showed the opposite trend as the 14-3-3ζ in complex with pPdc became more accessible for deuteration. However, this effect vanished later during the exchange reflecting dynamic behavior of this region.

Discussion

The main aim of this study is to provide a mechanistic insight into the regulation of Pdc by means of the 14-3-3-protein binding. Bioinformatics analysis revealed that more than 90% of the 14-3-3 binding partners contain intrinsically disordered segments, and the majority of the high affinity 14-3-3-binding motifs are located within these disordered regions (59, 60). The presence of the 14-3-3-binding motifs within flexible regions likely uncouples the binding strength from the specificity and renders these phosphorylation-dependent and highly specific interactions reversible. Structural studies of the Pdc·$G_t\beta\gamma$ complex suggested that Pdc is not an exception because Pdc-ND has been found to be highly flexible and poorly structured (13, 14). Theoretical prediction as well as biophysical characterization clearly showed that Pdc-ND, in contrast to the folded and compact Pdc-CD, is intrinsically unstructured and adopts a highly extended conformation (Figs. 1 and 2 and Table 1). The disordered and highly flexible nature of Pdc-ND was also confirmed by SAXS analysis, which revealed that solution structure of Pdc is best described as an ensemble of structurally variable conformers consisting of rigid Pdc-CD and flexible Pdc-ND (Figs. 3

and 4 and Table 2). In addition, Pdc-ND of unbound (apo) Pdc is significantly more extended compared with the conformation observed in the crystal structure of the Pdc·$G_t\beta\gamma$ complex (Fig. 4).

HDX-MS measurements revealed no dramatic disorder-to-order transition upon the pPdc binding to 14-3-3ζ, as no significant changes in deuteration kinetics of pPdc peptides were observed in the presence of 14-3-3ζ. However, small but significant reduction of flexibility was detected by time-resolved fluorescence measurements in regions containing Trp^{29}, Trp^{93} from Pdc-ND, and Trp^{208} from Pdc-CD (Fig. 5 and Table 3). Consistently, we also observed an increase in τ_{mean} as well as a decrease in the accessibility of these three tryptophan residues upon the complex formation (Tables 3 and 4) suggesting interaction between 14-3-3ζ and Pdc regions containing these residues. In contrast to Pdc, the 14-3-3ζ dimer offers a rigid and well defined binding surface as several peptides located both inside and outside the central channel exhibited significant decrease in deuterium incorporation upon the complex formation (Fig. 8). Therefore, it is reasonable to assume that pPdc-ND containing both phosphorylation sites binds into the central channel of 14-3-3ζ, whereas Pdc-CD interacts with regions located outside the central channel of the 14-3-3ζ dimer through the side containing Trp^{208} (Fig. 9) as this residue showed lower accessibility upon the complex formation, although the accessibility of Trp^{123} remained unaltered (Table 4).

SV AUC measurements revealed that pPdc-ND is responsible for the stability of the pPdc·14-3-3ζ complex as no significant binding was observed between the isolated Pdc-CD and 14-3-3ζ (Fig. 6). This suggests that the interaction between 14-3-3ζ and Pdc-CD is enabled by means of the local concentration effect upon the docking of pPdc-ND into the central channel of 14-3-3ζ. In this respect, the pPdc·14-3-3ζ complex resembles many other 14-3-3 protein complexes where the key interaction for protein association is the coordination of phosphorylated residue(s), and the interactions with regions remote from the phosphorylated 14-3-3-binding motif(s) by themselves are insufficient for stable complex formation. For example, associations of 14-3-3 with serotonin *N*-acetyltransferase (61), yeast neutral trehalase Nth1 (62), or forkhead transcription factor FOXO4 (63) are fully dependent on the phosphorylation of the 14-3-3-binding motif(s) despite extensive interactions beyond those involving the phosphorylated motifs and the 14-3-3 binding grooves.

The Pdc-ND constitutes the larger part of Pdc's interaction interface with $G_t\beta\gamma$, whereas Pdc-CD seems to be responsible for blocking the interaction of $G_t\beta\gamma$ with the membrane (13, 14). Thus, the binding interaction between 14-3-3ζ and pPdc-ND might either sterically block the Pdc's $G_t\beta\gamma$ binding surface and change its structure as well as decrease the rate of Pdc dephosphorylation after a light stimulus by virtue of its interaction with phosphorylated residues (9). In addition, contacts between 14-3-3ζ and the region containing Trp^{208} suggest that the 14-3-3ζ binding might also affect the C-terminal part of the $G_t\beta\gamma$ binding interface of pPdc (Fig. 1*A*) (13).

Taken together, the 14-3-3 protein dimer interacts with Pdc using surfaces both inside and outside its central channel. The N-terminal domain of Pdc, where both phosphorylation sites and the 14-3-3-binding motifs are located, is an intrinsically disordered protein that reduces its flexibility in several regions without undergoing dramatic disorder-to-order transition upon binding to 14-3-3. Our data also indicate that the C-terminal domain of Pdc interacts with the outside surface of the 14-3-3 dimer through the region involved in $G_t\beta\gamma$ binding. Therefore, we show that the 14-3-3 protein interacts with and sterically occludes both the N- and C-terminal Gt$\beta\gamma$ binding interfaces of phosphorylated Pdc, thus providing a mechanistic explanation for the 14-3-3-depedent inhibition of Pdc function.

Acknowledgments—The mass spectrometry facility was supported by Project CZ.2.16/3.1.00/24023. We acknowledge the use of analytical ultracentrifuge in Central European Institute of Technology in Brno, Czech Republic.

References

1. Lee, R. H., Lieberman, B. S., and Lolley, R. N. (1987) A novel complex from bovine visual cells of a 33,000-dalton phosphoprotein with β- and γ-transducin: purification and subunit structure. *Biochemistry* **26,** 3983–3990
2. Bauer, P. H., Müller, S., Puzicha, M., Pippig, S., Obermaier, B., Helmreich, E. J., and Lohse, M. J. (1992) Phosducin is a protein kinase A-regulated G-protein regulator. *Nature* **358,** 73–76
3. Zhu, X., and Craft, C. M. (2000) Modulation of CRX transactivation activity by phosducin isoforms. *Mol. Cell. Biol.* **20,** 5216–5226
4. Herrmann, R., Lobanova, E. S., Hammond, T., Kessler, C., Burns, M. E., Frishman, L. J., and Arshavsky, V. Y. (2010) Phosducin regulates transmission at the photoreceptor-to-ON-bipolar cell synapse. *J. Neurosci.* **30,** 3239–3253
5. Beetz, N., Harrison, M. D., Brede, M., Zong, X., Urbanski, M. J., Sietmann, A., Kaufling, J., Lorkowski, S., Barrot, M., Seeliger, M. W., Vieira-Coelho, M. A., Hamet, P., Gaudet, D., Seda, O., Tremblay, J., *et al.* (2009) Phosducin influences sympathetic activity and prevents stress-induced hypertension in humans and mice. *J. Clin. Invest.* **119,** 3597–3612
6. Willardson, B. M., and Howlett, A. C. (2007) Function of phosducin-like proteins in G protein signaling and chaperone-assisted protein folding. *Cell. Signal.* **19,** 2417–2427
7. Lee, R. H., Lieberman, B. S., Yamane, H. K., Bok, D., and Fung, B. K. (1992) A third form of the G protein β subunit. 1. Immunochemical identification and localization to cone photoreceptors. *J. Biol. Chem.* **267,** 24776–24781
8. Yoshida, T., Willardson, B. M., Wilkins, J. F., Jensen, G. J., Thornton, B. D., and Bitensky, M. W. (1994) The phosphorylation state of phosducin determines its ability to block transducin subunit interactions and inhibit transducin binding to activated rhodopsin. *J. Biol. Chem.* **269,** 24050–24057
9. Thulin, C. D., Savage, J. R., McLaughlin, J. N., Truscott, S. M., Old, W. M., Ahn, N. G., Resing, K. A., Hamm, H. E., Bitensky, M. W., and Willardson, B. M. (2001) Modulation of the G protein regulator phosducin by Ca^{2+}/calmodulin-dependent protein kinase II phosphorylation and 14-3-3 protein binding. *J. Biol. Chem.* **276,** 23805–23815
10. Nakano, K., Chen, J., Tarr, G. E., Yoshida, T., Flynn, J. M., and Bitensky, M. W. (2001) Rethinking the role of phosducin: light-regulated binding of phosducin to 14-3-3 in rod inner segments. *Proc. Natl. Acad. Sci. U.S.A.* **98,** 4693–4698
11. Lee, B. Y., Thulin, C. D., and Willardson, B. M. (2004) Site-specific phosphorylation of phosducin in intact retina. Dynamics of phosphorylation and effects on G protein βγ dimer binding. *J. Biol. Chem.* **279,** 54008–54017
12. Obsil, T., and Obsilova, V. (2011) Structural basis of 14-3-3 protein functions. *Semin. Cell Dev. Biol.* **22,** 663–672
13. Gaudet, R., Bohm, A., and Sigler, P. B. (1996) Crystal structure at 2.4 angstroms resolution of the complex of transducin βγ and its regulator,

phosducin. *Cell* **87,** 577–588
14. Gaudet, R., Savage, J. R., McLaughlin, J. N., Willardson, B. M., and Sigler, P. B. (1999) A molecular mechanism for the phosphorylation-dependent regulation of heterotrimeric G proteins by phosducin. *Mol. Cell* **3,** 649–660
15. Rezabkova, L., Kacirova, M., Sulc, M., Herman, P., Vecer, J., Stepanek, M., Obsilova, V., and Obsil, T. (2012) Structural modulation of phosducin by phosphorylation and 14-3-3 protein binding. *Biophys. J.* **103,** 1960–1969
16. Zhu, X., and Craft, C. M. (1998) Interaction of phosducin and phosducin isoforms with a 26S proteasomal subunit, SUG1. *Mol. Vis.* **4,** 13
17. Obsilova, V., Herman, P., Vecer, J., Sulc, M., Teisinger, J., and Obsil, T. (2004) 14-3-3ζ C-terminal stretch changes its conformation upon ligand binding and phosphorylation at Thr^{232}. *J. Biol. Chem.* **279,** 4531–4540
18. Obsilova, V., Nedbalkova, E., Silhan, J., Boura, E., Herman, P., Vecer, J., Sulc, M., Teisinger, J., Dyda, F., and Obsil, T. (2008) The 14-3-3 protein affects the conformation of the regulatory domain of human tyrosine hydroxylase. *Biochemistry* **47,** 1768–1777
19. Kosek, D., Kylarova, S., Psenakova, K., Rezabkova, L., Herman, P., Vecer, J., Obsilova, V., and Obsil, T. (2014) Biophysical and structural characterization of the thioredoxin-binding domain of protein kinase ASK1 and its interaction with reduced thioredoxin. *J. Biol. Chem.* **289,** 24463–24474
20. Schuck, P. (2000) Size-distribution analysis of macromolecules by sedimentation velocity ultracentrifugation and lamm equation modeling. *Biophys. J.* **78,** 1606–1619
21. Dam, J., Velikovsky, C. A., Mariuzza, R. A., Urbanke, C., and Schuck, P. (2005) Sedimentation velocity analysis of heterogeneous protein-protein interactions: Lamm equation modeling and sedimentation coefficient distributions *c*(*s*). *Biophys. J.* **89,** 619–634
22. Roessle, M. W., Klaering, R., Ristau, U., Robrahn, B., Jahn, D., Gehrmann, T., Konarev, P., Round, A., Fiedler, S., Hermes, C., and Svergun, D. (2007) Upgrade of the small-angle X-ray scattering beamline X33 at the European Molecular Biology Laboratory, Hamburg. *J. Appl. Crystallogr.* **40,** S190–S194
23. Guinier, A. (1939) La diffraction des rayons X aux très faibles angles: Applications à l'etude des phénomènes ultra-microscopies. *Ann. Phys.* **12,** 161–237
24. Svergun, D. I. (1992) Determination of the regularization parameter in indirect-transform methods using perceptual criteria. *J. Appl. Crystallogr.* **25,** 495–503
25. Svergun, D. I. (1999) Restoring low resolution structure of biological macromolecules from solution scattering using simulated annealing. *Biophys. J.* **76,** 2879–2886
26. Volkov, V. V., and Svergun, D. I. (2003) Uniqueness of *ab initio* shape determination in small-angle scattering. *J. Appl. Crystallogr.* **36,** 860–864
27. Bernadó, P., Mylonas, E., Petoukhov, M. V., Blackledge, M., and Svergun, D. I. (2007) Structural characterization of flexible proteins using small-angle x-ray scattering. *J. Am. Chem. Soc.* **129,** 5656–5664
28. Vecer, J., Vesela, P., Malinsky, J., and Herman, P. (2014) Sphingolipid levels crucially modulate lateral microdomain organization of plasma membrane in living yeast. *FEBS Lett.* **588,** 443–449
29. Vecer, J., and Herman, P. (2011) Maximum entropy analysis of analytically simulated complex fluorescence decays. *J. Fluoresc.* **21,** 873–881
30. Cross, A. J., and Fleming, G. R. (1984) Analysis of time-resolved fluorescence anisotropy decays. *Biophys. J.* **46,** 45–56
31. Gilbert, C. W. (1983) in *Time-resolved Fluorescence Spectroscopy in Biochemistry and Biology* (Cundall, R. B., and Dale, R. E., eds) pp. 605–606, Plenum Press, New York
32. Eftink, M. R., and Ghiron, C. A. (1976) Exposure of tryptophanyl residues in proteins–quantitative-determination by fluorescence quenching studies. *Biochemistry* **15,** 672–680
33. Lakowicz, J. R. (1999) *Principles of Fluorescence Spectroscopy,* 2nd Ed., pp. 53–55, Kluwer Academic/Plenum Publishers, New York
34. Trcka, F., Durech, M., Man, P., Hernychova, L., Muller, P., and Vojtesek, B. (2014) The assembly and intermolecular properties of the Hsp70-Tomm34-Hsp90 molecular chaperone complex. *J. Biol. Chem.* **289,** 9887–9901
35. Loew, A., Ho, Y. K., Blundell, T., and Bax, B. (1998) Phosducin induces a structural change in transducin $\beta\gamma$. *Structure* **6,** 1007–1019
36. Obradovic, Z., Peng, K., Vucetic, S., Radivojac, P., Brown, C. J., and Dunker, A. K. (2003) Predicting intrinsic disorder from amino acid sequence. *Proteins* **53,** 566–572
37. Ward, J. J., Sodhi, J. S., McGuffin, L. J., Buxton, B. F., and Jones, D. T. (2004) Prediction and functional analysis of native disorder in proteins from the three kingdoms of life. *J. Mol. Biol.* **337,** 635–645
38. Dosztányi, Z., Csizmok, V., Tompa, P., and Simon, I. (2005) IUPred: web server for the prediction of intrinsically unstructured regions of proteins based on estimated energy content. *Bioinformatics* **21,** 3433–3434
39. Xue, B., Dunbrack, R. L., Williams, R. W., Dunker, A. K., and Uversky, V. N. (2010) PONDR-FIT: a meta-predictor of intrinsically disordered amino acids. *Biochim. Biophys. Acta* **1804,** 996–1010
40. Uversky, V. N. (2002) What does it mean to be natively unfolded? *Eur. J. Biochem.* **269,** 2–12
41. Footer, M. J., Lyo, J. K., and Theriot, J. A. (2008) Close packing of *Listeria monocytogenes* ActA, a natively unfolded protein, enhances F-actin assembly without dimerization. *J. Biol. Chem.* **283,** 23852–23862
42. Murray, C. L., Marcotrigiano, J., and Rice, C. M. (2008) Bovine viral diarrhea virus core is an intrinsically disordered protein that binds RNA. *J. Virol.* **82,** 1294–1304
43. Hotta, K., Ranganathan, S., Liu, R., Wu, F., Machiyama, H., Gao, R., Hirata, H., Soni, N., Ohe, T., Hogue, C. W., Madhusudhan, M. S., and Sawada, Y. (2014) Biophysical properties of intrinsically disordered p130Cas substrate domain–implication in mechanosensing. *PLoS Comput. Biol.* **10,** e1003532
44. Woody, R. W. (2010) in *Instrumental Analysis of Intrinsically Disordered Proteins: Assessing Structure and Conformation* (Uversky, V. N., and Longhi, S., eds) pp. 303–321, John Wiley & Sons, Hoboken, NJ
45. Uversky, V. N., Winter, S., and Löber, G. (1996) Use of fluorescence decay times of 8-ANS-protein complexes to study the conformational transitions in proteins which unfold through the molten globule state. *Biophys. Chem.* **60,** 79–88
46. Bernadó, P., and Svergun, D. I. (2012) Structural analysis of intrinsically disordered proteins by small-angle x-ray scattering. *Mol. Biosyst.* **8,** 151–167
47. Kopecka, M., Kosek, D., Kukacka, Z., Rezabkova, L., Man, P., Novak, P., Obsil, T., and Obsilova, V. (2014) Role of the EF-hand-like motif in the 14-3-3 protein-mediated activation of yeast neutral trehalase Nth1. *J. Biol. Chem.* **289,** 13948–13961
48. Putnam, C. D., Hammel, M., Hura, G. L., and Tainer, J. A. (2007) X-ray solution scattering (SAXS) combined with crystallography and computation: defining accurate macromolecular structures, conformations and assemblies in solution. *Q. Rev. Biophys.* **40,** 191–285
49. Mertens, H. D., and Svergun, D. I. (2010) Structural characterization of proteins and complexes using small-angle x-ray solution scattering. *J. Struct. Biol.* **172,** 128–141
50. Bernadó, P. (2010) Effect of interdomain dynamics on the structure determination of modular proteins by small-angle scattering. *Eur. Biophys. J.* **39,** 769–780
51. Silhan, J., Obsilova, V., Vecer, J., Herman, P., Sulc, M., Teisinger, J., and Obsil, T. (2004) 14-3-3 protein C-terminal stretch occupies ligand binding groove and is displaced by phosphopeptide binding. *J. Biol. Chem.* **279,** 49113–49119
52. Bajzer, Z., and Prendergast, F. G. (1993) A model for multiexponential tryptophan fluorescence intensity decay in proteins. *Biophys. J.* **65,** 2313–2323
53. Chen, Y., and Barkley, M. D. (1998) Toward understanding tryptophan fluorescence in proteins. *Biochemistry* **37,** 9976–9982
54. Truong, A. B., Masters, S. C., Yang, H., and Fu, H. (2002) Role of the 14-3-3 C-terminal loop in ligand interaction. *Proteins* **49,** 321–325
55. Ottmann, C., Marco, S., Jaspert, N., Marcon, C., Schauer, N., Weyand, M., Vandermeeren, C., Duby, G., Boutry, M., Wittinghofer, A., Rigaud, J. L., and Oecking, C. (2007) Structure of a 14-3-3 coordinated hexamer of the plant plasma membrane H^+-ATPase by combining x-ray crystallography and electron cryomicroscopy. *Mol. Cell* **25,** 427–440
56. Rezabkova, L., Man, P., Novak, P., Herman, P., Vecer, J., Obsilova, V., and Obsil, T. (2011) Structural basis for the 14-3-3 protein-dependent inhibi-

tion of the regulator of G protein signaling 3 (RGS3) function. *J. Biol. Chem.* **286,** 43527–43536
57. Engen, J. R. (2003) Analysis of protein complexes with hydrogen exchange and mass spectrometry. *Analyst* **128,** 623–628
58. Macakova, E., Kopecka, M., Kukacka, Z., Veisova, D., Novak, P., Man, P., Obsil, T., and Obsilova, V. (2013) Structural basis of the 14-3-3 protein-dependent activation of yeast neutral trehalase Nth1. *Biochim. Biophys. Acta* **1830,** 4491–4499
59. Bustos, D. M. (2012) The role of protein disorder in the 14-3-3 interaction network. *Mol. Biosyst.* **8,** 178–184
60. Collins, M. O., Yu, L., Campuzano, I., Grant, S. G., and Choudhary, J. S. (2008) Phosphoproteomic analysis of the mouse brain cytosol reveals a predominance of protein phosphorylation in regions of intrinsic sequence disorder. *Mol. Cell. Proteomics* **7,** 1331–1348
61. Obsil, T., Ghirlando, R., Klein, D. C., Ganguly, S., and Dyda, F. (2001) Crystal structure of the 14-3-3ζ:serotonin *N*-acetyltransferase complex. A role for scaffolding in enzyme regulation. *Cell* **105,** 257–267
62. Veisova, D., Macakova, E., Rezabkova, L., Sulc, M., Vacha, P., Sychrova, H., Obsil, T., and Obsilova, V. (2012) Role of individual phosphorylation sites for the 14-3-3-protein-dependent activation of yeast neutral trehalase Nth1. *Biochem. J.* **443,** 663–670
63. Obsil, T., Ghirlando, R., Anderson, D. E., Hickman, A. B., and Dyda, F. (2003) Two 14-3-3 binding motifs are required for stable association of Forkhead transcription factor FOXO4 with 14-3-3 proteins and inhibition of DNA binding. *Biochemistry* **42,** 15264–15272
64. Yaffe, M. B., Rittinger, K., Volinia, S., Caron, P. R., Aitken, A., Leffers, H., Gamblin, S. J., Smerdon, S. J., and Cantley, L. C. (1997) The structural basis for 14-3-3:phosphopeptide binding specificity. *Cell* **91,** 961–971
65. Eftink, M. R., and Ghiron, C. A. (1976) Fluorescence quenching of indole and model micelle systems. *J. Phys. Chem.* **80,** 486–493